

<https://doi.org/10.1038/s43246-024-00558-5>

# Ultra-fast perovskite electro-optic modulator and multi-band transmission up to 300 Gbit s<sup>-1</sup>



Jiawei Mao<sup>1</sup>, Futa Uemura<sup>2</sup>, Sahar Alasvand Yazdani<sup>1</sup>, Yuexin Yin<sup>1</sup>, Hiromu Sato<sup>1</sup>, Guo-Wei Lu<sup>1,2</sup> & Shiyoshi Yokoyama<sup>1,2</sup>

The gap between the performance of optoelectronic components and the demands of fiber-optic communications has narrowed significantly in recent decades. Yet, the expansion of data communications traffic remains substantial, with fiber-link speeds increases anticipated in the near future. Here, we demonstrate an ultra-high-speed electro-optic waveguide modulator constructed using a thin film of lanthanum-modified lead zirconate titanate with a ferroelectric phase exhibiting a strong Pockels effect. The modulator has a wide optical window; thus, the modulation was demonstrated for 1550 and 1310 nm wavelengths. This device showed electro-optical intensity signaling with line rates of 172 Gbit s<sup>-1</sup>, in conjunction with on-off keying modulation; this performance could be increased to 304 Gbit s<sup>-1</sup> using four-level pulse modulation. The signaling performance of this modulator was found to be robust, with stable performance at temperatures as high as 100 °C. This technology is expected to have applications in a wide range of classical optoelectronic devices and in quantum science and technology.

The recent emergence of bandwidth-intensive applications such as high-resolution streaming media, 5G, cloud-based service delivery, and the Internet of Things has greatly increased the required data transmission rates. This rapid increase highlights the urgent need to develop optoelectronic signaling systems that provide high data transmission rates via fiber-optic communications. Future challenges related to such systems will involve the design of high-speed modulation technologies. Among the various types of optoelectronic modulation formats based on different physical mechanisms, the first-order electro-optic (EO) phenomenon known as the Pockels effect has recently received much attention<sup>1–5</sup>. This interest is related to the substantial increase in reports of materials that exhibit a strong Pockels effects and that enable efficient EO modulation with high-speed line rates. Recent advances in EO modulators have also led to the rapid development of efficient EO waveguide devices comprising ferroelectric thin films on silicon oxide/silicon (SiO<sub>2</sub>/Si) substrates. These devices have enabled new microwave-based photonics applications<sup>1,4,5</sup>.

In previous studies, lithium niobate (LN) thin films fabricated on insulators were shown to have applications in devices such as photonic integrated circuits<sup>6–8</sup>. In particular, state-of-the-art LN devices that take advantage of efficient modulation to realize low-voltage drive in conjunction with a small footprint have potential applications as tunable rings, Mach-Zehnder interferometers (MZIs), and other nonlinear optical

devices. Such modulators have demonstrated large modulation bandwidths, enabling nearly 100 Gbaud signaling with error-free transmission<sup>1,5,9</sup>. However, the limited EO coefficient of approximately 31 pm V<sup>-1</sup> for such devices makes improving the modulation efficiency while further reducing size difficult. An alternative approach is to take advantage of the large EO effect of organic polymers, which exhibit exceptional modulation efficiency in the high-frequency range<sup>10–12</sup>. These materials also have potential applications in various hybrid Si photonics and plasmonic photonics structures. In fact, the progress to date in the study of organic polymer modulators suggests that these materials could offer a rare means of achieving data modulations higher than 100 GBD<sup>11</sup> and line rates beyond 200 Gbit s<sup>-1</sup><sup>1,12–14</sup>, thereby meeting the requirements for applications such as short-reach and data-center optical interconnects. However, concerns about reliability persist, particularly regarding the material's resistance to high temperatures and susceptibility to photobleaching damage under an ambient atmosphere. Further investigations to ensure that these concepts are suitable for industrial applications are ongoing<sup>12,15,16</sup>.

Perovskite crystals with ferroelectricity, such as KNbO<sub>3</sub><sup>17,18</sup>, Pb[Zr,Ti]O<sub>3</sub> (PZT)<sup>19</sup>, BaTiO<sub>3</sub> (BTO)<sup>20,21</sup>, and PbTiO<sub>3</sub><sup>22</sup>, are being explored for extensive applications in nonlinear optical devices because of their substantial EO coefficients on the order of 10<sup>2</sup> pm V<sup>-1</sup>. The key advantages of EO materials include a linear correlation between the change in refractive

<sup>1</sup>Institute for Materials Chemistry and Engineering, Kyushu University, 6-1 Kasuga-koen Kasuga, Fukuoka 816-8580, Japan. <sup>2</sup>Department of Molecular and Material Science, Kyushu University, 6-1 Kasuga-koen Kasuga, Fukuoka 816-8580, Japan. e-mail: s\_yokoyama@cm.kyushu-u.ac.jp

index and the applied electric field, fast response, and control of light propagation, all of which are critical to the application of waveguide modulators. Recently, ferroelectric EO modulators fabricated on insulating substrates have demonstrated high degrees of optical modulation to provide relatively short phase shifters or small microrings that require low drive voltages compared with previous crystal modulators<sup>2,4,23,24</sup>. The formation of ferroelectric domains is a vital aspect of the fabrication of these devices, whether using sputtering, pulsed laser deposition, or molecular beam epitaxy techniques. In early works, the heterogeneous integration of thin ferroelectric films and their transfer onto the optic structures led to Si-based photonics platforms having superior EO characteristics<sup>2,4,24</sup>. Some platforms with superior performance have been reported when BTO is used in this regard because this material has one of the highest EO coefficients among the various perovskite ferroelectric crystals. For example, the reported drive voltages, or  $V_{\pi}L$  values (the product of the half-wave voltage ( $V_{\pi}$ ) and the phase-shifter length ( $L$ )), for the EO modulators are an order of magnitude smaller than those reported for other Si carrier dispersion-type modulators and are comparable to those exhibited by integrated semiconductor capacitor modulators<sup>25</sup>. The EO effect in perovskites originates from the non-centrosymmetry of poled electric polarization. A relatively large remanent dipole and coercive field are their advantageous features<sup>20,26,27</sup>. Despite their attractive EO properties, temperature sensitivity of the crystal lattice or orientation due to thermal phase transmission is a challenge for their industrial application<sup>2,4,28</sup>. Perovskites with higher phase-transition temperatures and Curie temperatures ( $T_c$ s) are therefore preferred for use in thermally stable photonic devices. In the case of perovskite modulators, high-speed signaling at approximately 25–56 Gbit s<sup>-1</sup> has previously been demonstrated in MZI or ring modulators with a modulation bandwidth of ~30 GHz<sup>4,24,29</sup>. Only plasmonic structures have demonstrated a higher signaling speed (~70 Gbit s<sup>-1</sup>)<sup>30</sup>. However, further expansion of the signaling speed is expected to be possible with the next-generation transmitter technology.

In the present work, we fabricated La-modified-PZT ([Pb,La][Zr,Ti]O<sub>3</sub>, PLZT) thin films and traveling-wave MZI modulators to demonstrate efficient and stable EO modulation and high-speed transmission. This material, which exhibits an enhanced EO coefficient compared with PZT or other previously reported ferroelectric crystals, was selected for its advantages of a high phase-transition temperature, strong poled polarization, and high remanent polarization<sup>26,31</sup>. The PLZT films were prepared on SiO<sub>2</sub>/Si substrates by simple solution spin coating and thermal annealing techniques. The crystals resulted in the SiO<sub>2</sub>-stacked photonic layer exhibiting an enhanced high-frequency response, which is a prerequisite for achieving high-speed EO modulators. Unlike modulators prepared with other crystals<sup>21</sup>, our modulators do not exhibit de-poling relaxation. Consequently, a DC poling bias does not need to be applied during the modulation. Our modulator has an expanded optical window at wavelengths near the infrared region. The measured  $V_{\pi}L$  values for this modulator were 7.0 V·mm at a wavelength of 1550 nm and 5.6 V·mm at 1310 nm. The EO modulator demonstrated stable resistance with little change in modulation efficiency even after being exposed to elevated temperatures. EO modulation was demonstrated with a large frequency bandwidth, indicating superior high-speed modulation performance. The optical signal transmission was attained, with line rates as high as 172 Gbit s<sup>-1</sup> in the on-off keying (OOK) signal format and 304 Gbit s<sup>-1</sup> in conjunction with the four-level pulse-amplitude modulation (PAM4) signal format.

## Results

### Deposition of PLZT

The first step was the deposition of a PLZT film onto a SiO<sub>2</sub>/Si substrate. The literature contains few reports on the preparation of perovskite EO films on a SiO<sub>2</sub> surface, which might be a necessary component for photonic waveguide applications. Certain perovskites with ferroelectric phases oriented along the *c*-axis can be prepared on a crystalline surface only if a suitable intermediate layer is first applied<sup>32–34</sup>. A lanthanide-based intermediate layer has shown promise in this regard and has been found to lead

to La<sub>2</sub>O<sub>2</sub>CO<sub>3</sub> having a prominent out-of-plane tetragonal phase-oriented along the *c*-axis, with lattice parameters of  $a = 4.07$  Å and  $c = 13.49$  Å<sup>35</sup>. We found, in the present study, that this layer is useful when used as an intermediate layer on a SiO<sub>2</sub> surface to form *c*-axis-oriented PLZT. The deposition of PLZT began with spin coating of an intermediate layer onto a SiO<sub>2</sub>/Si substrate using a solution of lanthanum nitrate (La(NO<sub>3</sub>)<sub>3</sub>) in 2-methoxyethanol. The thickness of the thermally oxidized SiO<sub>2</sub> was 2.0 µm. The SiO<sub>2</sub> surface was initially covered with polyvinylpyrrolidone to enhance the uniformity of the applied La(NO<sub>3</sub>)<sub>3</sub>. Heating the spin-coated film at 500 °C gave an intermediate layer less than 10 nm thick. The precursor sol-gel solution of PLZT was then spin-coated on top of the intermediate layer, followed by heating at 300 °C. Each such cycle of spin coating and heating generated a ~100 nm-thick film, and this cycle could be repeated to obtain films with specific thicknesses. Finally, the film was annealed at 600 °C under a flow of O<sub>2</sub> to generate crystalline PLZT. The obtained PLZT films were characterized by X-ray diffraction (XRD) measurements using the  $\theta$ -2 $\theta$  technique. A typical diffraction pattern is displayed in Fig. 1a. The measured 2 $\theta$  represents the diffraction angle relative to the incident beam, where  $\theta$  is the Bragg angle for the crystal. The strong peaks at 2 $\theta$  = 21.95° and 44.72° correspond to the (100) and (200) planes, respectively. These peaks are indicative of a ferroelectric domain that possesses either a tetragonal or rhombohedral structure. This result is attributed to the good lattice match between the PLZT (lattice constant  $a = 4.05$  Å) and the La<sub>2</sub>O<sub>2</sub>CO<sub>3</sub>. In addition to the choice of the intermediate layer, parameters such as the O<sub>2</sub> flow rate and the substrate temperature strongly influence the crystalline orientation. Comparing the XRD patterns reveals that annealing under O<sub>2</sub> preferentially promoted the growth of the ferroelectric phase with a (100) orientation (Supplementary Fig. 1).

### PLZT modulator

The deposited PLZT films exhibited a random in-plane dipolar orientation with respect to the surface normal. Thus, these films did not show the EO effect. Electric poling is required to induce the dipolar characteristic of the ferroelectric state. Such a poling process is a critical aspect of using these PLZT films for EO modulator applications. Metal electrodes were deposited across the PLZT waveguide and used for both poling and modulation. A cross-sectional schematic of the PLZT modulator is shown in Fig. 1b. Notably, the waveguide was designed such that the optical confinement (defined here as the ratio of optical electric field power within the PLZT region to the total guided mode power) was maximized to enable efficient EO modulation. This maximization was accomplished by patterning a ridge-shaped waveguide on a 300 nm-thick PLZT film. The width ( $W_{wg}$ ) and height ( $H_{rid}$ ) of these ridges were 1.5 µm and 100 nm, respectively. Figure 1c presents a scanning electron microscopy image of this waveguide. Finally, the MZI unit was fabricated, as shown in the overhead-view image in Fig. 1d. In this device, the incoming laser beam was split into two waveguides via a 1 × 2 multimode interference (MMI) and then conducted to the 2.5 mm-long phase shifters. The electrode had a coplanar ground–signal–ground (GSG) configuration that enabled electric signals to be applied to each phase shifter to demonstrate push–pull MZI operation. In the phase-shifter section, the electric field was applied along the plane of the surface; thus, the optical transmission was designed to operate in the transverse electromagnetic (TE) mode. Figure 1e shows the calculated electric field distribution associated with the TE<sub>0</sub> mode. Because of the higher refractive index of PLZT compared with that of SiO<sub>2</sub>, the upper and lower claddings limited longitudinal mode propagation, resulting in a focused optical mode in the PLZT layer and providing an estimated confinement factor of 73%. The simulation-designed waveguides, confinement factors, and MMIs are shown in Supplementary Figs. 2 and 3. This study employed a high-temperature poling technique to activate the PLZT modulator. Prior to poling, the modulator did not exhibit any EO effect because of the absence of polarization. An electric field of 18 V µm<sup>-1</sup> was applied between the electrodes at 90 °C. This field was almost three times greater than the coercive field value reported for PLZT and was sufficiently high to complete the poling process (Supplementary Fig. 4). After the device

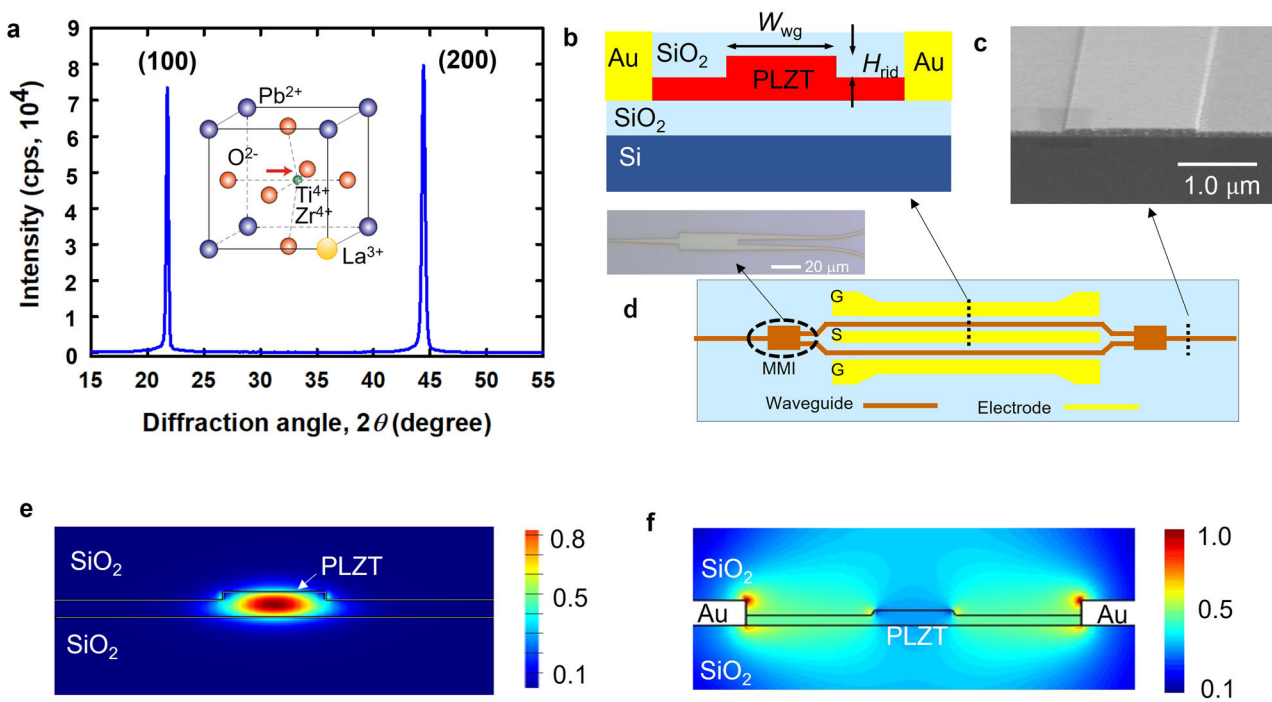
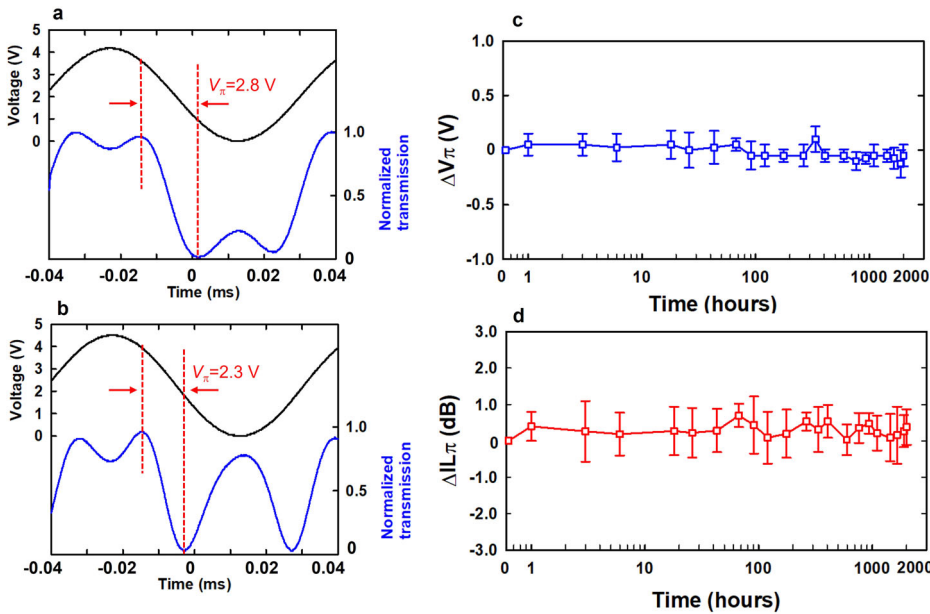


**Fig. 1 | PLZT film and modulator.** **a** XRD pattern for a 200 nm-thick PLZT film prepared on a SiO<sub>2</sub>/Si substrate whose surface was coated with an intermediate layer. **b** Schematic showing the cross-section of the phase-shifter part of the modulator. **c** Angled scanning electron microscopy image of the PLZT waveguide. **d** Schematic

overhead view of a PLZT modular chip. Inset: magnified optical image of the MMI section. **e** Simulation of the optical electric field distribution along a cross-section of the PLZT waveguide. **f** Simulated RF electric field distribution.

**Fig. 2 | EO properties of the PLZT modulator.** **a, b**  $V_\pi$  values for the device, where the intensity-modulated signals (blue) driven by a 14 kHz sinusoidal electrical signal (black) at 1550 (a) and 1310 nm (b), respectively, are shown. **c, d**  $V_\pi$  and optical insertion loss data, respectively, acquired from the PLZT modulator at 85 °C for 2000 h. Error bars indicate multiple sample variations.

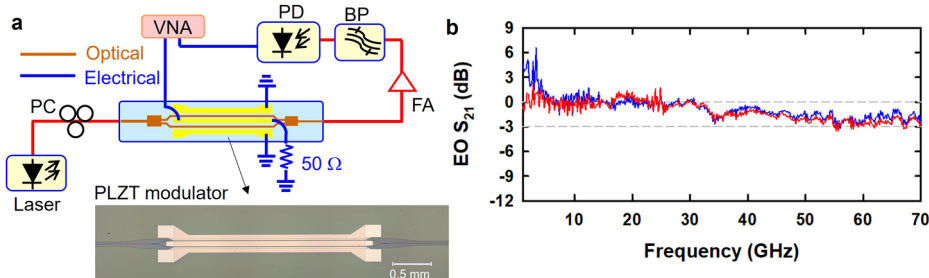


was cooled to room temperature and the poling voltage was removed, the polarization of the PLZT was frozen. No further application of a DC poling bias was required during modulator operation.

To optimize modulation,  $V_\pi$  values for the PLZT modulator were determined at wavelengths of 1550 and 1310 nm to ensure high EO efficiency. In the present work, laser light was guided to the modulator in conjunction with TE polarization via a polarization-maintaining fiber. Low-frequency data were acquired by applying a 14 kHz sinusoidal electrical signal to the modulator. The modulated light was received by a photodetector and recorded as an electrical signal using an oscilloscope. The

electrical and optical responses in Fig. 2a indicate that a  $V_\pi$  value of 2.8 V was obtained at 1550 nm, corresponding to  $V_\pi L = 7.0$  V·mm. The PLZT used in this work was transparent in the near-infrared region, enabling EO modulation at 1330 nm. From Fig. 2b, a  $V_\pi$  of 2.3 V can be obtained, corresponding to  $V_\pi L = 5.8$  V·mm. The high efficiency and poling DC-free modulation of this device are characteristic of our PLZT modulator and are typically not exhibited by other ferroelectric modulators. To confirm the stabilized modulation, we carried out a thermal and temporal stability test on the PLZT modulator. Figure 2c shows a plot of the change in  $V_\pi$  over time, as obtained from a trial in which the device was heated in air with

**Fig. 3 | Frequency response of the PLZT modulator.** **a**, Diagram of the experimental setup for measuring the EO bandwidth (i.e., the  $S_{21}$  parameter) for the PLZT modulator (inset photograph). **b**, EO  $S_{21}$  values demonstrating a bandwidth larger than 70 GHz.



measurements recorded at specific time intervals. The results confirm that the static EO effect for this PLZT modulator remained consistent at 85 °C for a time span of 2000 h. In addition, Fig. 2d establishes that the insertion loss showed no variation when the temperature was varied. Notably, testing at 85 °C was important to ensure the industrial-grade reliability necessary for optoelectronic devices.

### High-speed modulation

Perovskite ferroelectric crystals typically possess large dielectric constants, which can present challenges with regard to using these materials as traveling-wave modulators in modern high-speed optical communication systems. The modulation bandwidth of such devices is mainly limited by the impedance mismatch with the external device and source, the microwave velocity mismatch with the optical wave, and the signal propagation loss<sup>36</sup>. However, as previously demonstrated in works using ferroelectric film-on-insulator waveguides that showed improved modulation frequencies, the use of a SiO<sub>2</sub>/Si-stack waveguide can help mitigate these issues<sup>5,8,11</sup>.

Simulated optical and microwave electric field distributions for the present device are shown in Fig. 1e, f, respectively. Because the high optical confinement was focused around the PLZT ridge, optimized overlap between the microwave and optical distributions was expected to occur between the metal electrodes. In the case of high-frequency signaling in the gigahertz range, traveling-wave modulation is required to efficiently conduct the microwave signal to the phase shifter with minimal loss of the electro-optical response. The metal electrode fabricated on the PLZT modulator was composed of two parts: microstrip lines on the waveguide, and terminal pads. The coplanar electrode configuration (ground–signal–ground) also facilitated the smooth conduction of radiofrequency (RF) signals to the device via RF probes. The frequency response of the EO modulation was evaluated from 1 to 70 GHz using a vector network analyzer, as shown in the experimental setup in Fig. 3a.

The measurement results when small RF signals were applied to the modulator are shown in Fig. 3b. We measured a wide range of EO responses at frequencies as high as 70 GHz. However, the EO response changed sharply between 1 and 8 GHz, as indicated by the blue line. This RF response is attributable to parasitic surface conduction in the SiO<sub>2</sub>/Si substrate, which is a common issue in RF coplanar devices<sup>37</sup>. To mitigate such RF power attenuation, using substrates with a trap-rich passivation layer on Si might be effective<sup>38</sup>. In consideration of this reason, it was found that by compensating for the electrical properties in the low-frequency region, a broad frequency response from 1 to 70 GHz could be achieved in the EO modulation, as indicated by the red line response. The EO response in the high-frequency range was successfully maintained.

We examined the feasibility of using this PLZT modulator for high-speed transmission by producing OOK signals with line rates as high as 172 Gbit s<sup>-1</sup> using an arbitrary waveform generator (AWG). The modulated optical light was guided to a high-speed photodetector after passing through a fiber amplifier and a bandpass filter. This signal was then fed to a high-speed oscilloscope for eye-pattern generation. The measurement setup used for these experiments is illustrated in Fig. 4a; the measured eye patterns acquired at 172 Gbit s<sup>-1</sup> at 1550 nm are presented in Fig. 4b. The Q factor was estimated to be 2.99 from the results, where no equalization processes were used. The eye pattern shown in Fig. 4c was obtained when four-tap feedforward equalization (FFE) was applied within the digital

communication analyzer. Applying the FFE effectively increased the signal quality, as indicated by a Q factor of 4.17. As expected, no substantial differences were observed at a wavelength of 1310 nm. Figure 4d, e provide eye patterns obtained at 172 Gbit s<sup>-1</sup> OOK without and with the FFE, respectively; the corresponding Q factors were 3.0 and 4.0, respectively.

We further assessed the modulation performance of the proposed system by plotting the bit error ratio (BER) at various operating rates in Fig. 4h while maintaining a constant drive voltage of 200 mV<sub>pp</sub>, thereby enabling a direct comparison. The decrease in BER was enhanced with post-processing of the FFE. For analysis purposes, references were made using the hard-decision forward error correction (HD-FEC) and the soft-decision forward error correction (SD-FEC). The resultant BERs obtained without the FFE were below the HD-FEC at OOK rates as high as 172 Gbit s<sup>-1</sup>. The decrease in the BER was enhanced with post-processing of the FFE. These results are far below the HD-FEC. No differences in signal fidelity would be expected at wavelengths between 1550 and 1310 nm.

The observed device characteristics, including the phase-shifter length, drive voltage, and signal speed, would be expected to substantially improve the performance of state-of-the-art EO modulators. The Pockels-effect-induced EO response of the present perovskite modulator exhibits a linear relationship between electrical and optical power. As such, this modulation technique would likely be suitable for use in a multilevel signal format. In PAM4 systems, a four-level electrical signal is generated using an AWG as a digital-to-analog converter. This signal is then used to drive the PLZT modulator, achieving line rates from 232 to 304 Gbit s<sup>-1</sup>. To reduce the nonlinearity of the RF driver, the PAM4 modulations were tested with a lower voltage swing of 200 mV<sub>pp</sub>. At high line rates such as these and when working in the PAM4 format, employing Nyquist pulse shaping with a small roll-off factor of 0.1 can further enhance transmission, thus improving signaling efficiency. When the PLZT modulator was operated with a PAM4 modulation at a line rate of 304 Gbit s<sup>-1</sup>, BERs satisfying the HD-FEC threshold of less than  $4.5 \times 10^{-3}$  were recorded at both 1550 and 1310 nm (Fig. 4i). The corresponding eye patterns are shown in Fig. 4f, g. Transmissions at PAM4 rates between 200 and 280 Gbit s<sup>-1</sup> gave BERs better than the HD-SEC values. Notably, the EO modulation during these high-speed signaling tests was limited by the bandwidth and electric linearity of the available testing equipment. The factor that strongly affected the modulation amplitude was the voltage swing after the RF driver; this device can potentially provide better signaling fidelity and higher line rates than reported herein.

### Stable high-speed operation at elevated temperatures

We evaluated the transmission stability at elevated temperatures. PLZT typically shows exceptional ferroelectric thermal resistance based on a high-temperature phase transition and Curie transition<sup>31</sup> and was expected to exhibit thermally stable EO responses in the present study. In fact, the static electro-optic parameter,  $V_{ns}$ , and the insertion loss of the PLZT modulator reached constant, stable values over an extended duration during tests at 85 °C, as indicated by Fig. 2a, b. The ferroelectric phase of the PLZT was thermally stable at temperatures as high as 110 °C, as indicated by the temperature dependence of the XRD patterns in Supplementary Fig. 5.

The temperature sensitivity of the devices strongly affects the modulation accuracy during high-speed operation. Previously, reliable high-

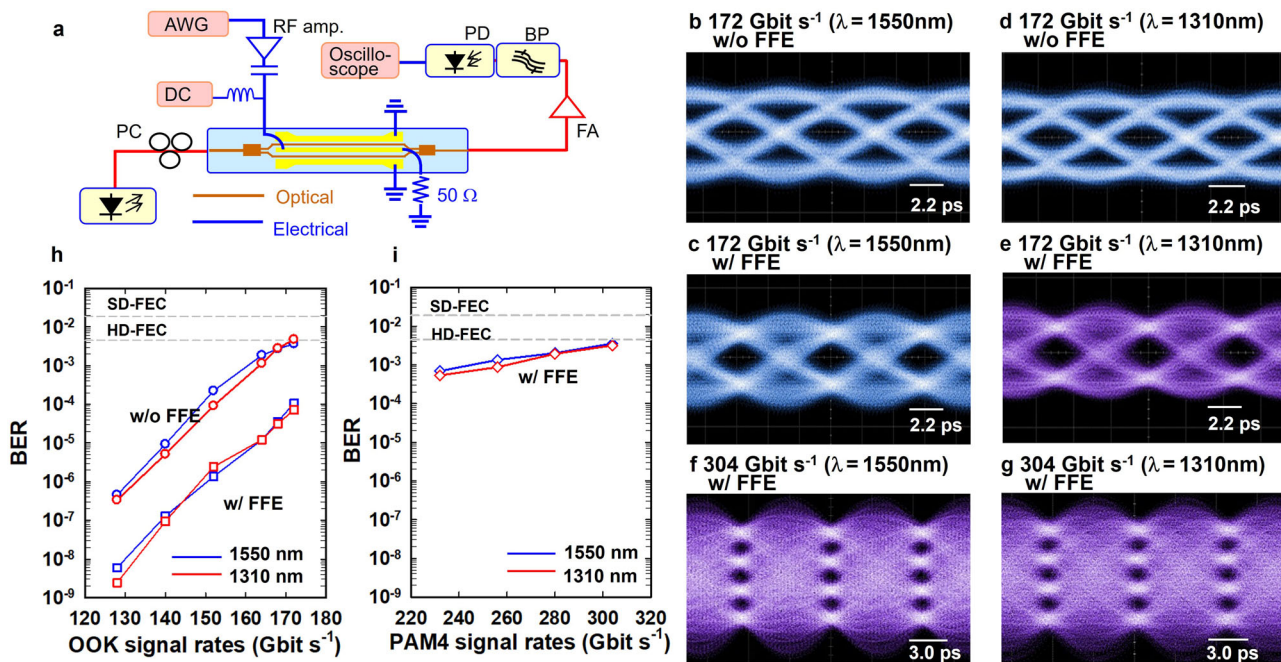


**Fig. 4 | High-speed transmission.** **a** The experimental setup used to obtain OOK and PAM4 signals from the PLZT modulator. This setup comprised an arbitrary waveform generator (AWG), an amplifier (amp), a DC voltage supplier, a polarization controller (PC), a fiber amplifier (FA), a bandpass filter (BP), and a photo-detector (PD). **b, c** Eye diagrams obtained from OOK signals at 172 Gbit s<sup>-1</sup> without FFE and with FFE (TAP = 4) for 1550 nm. **d, e** Eye diagrams obtained from OOK

signals at 172 Gbit s<sup>-1</sup> without FFE and with FFE (TAP = 4) for 1310 nm. **f, g** Eye diagrams obtained from PAM4 signals at 304 Gbit s<sup>-1</sup> for 1510 and 1310 nm. **h** BER values at different OOK signals and wavelengths for line rates of 128–172 Gbit s<sup>-1</sup>. **i** BER values at different PAM4 signals and wavelengths for line rates of 232 to 304 Gbit s<sup>-1</sup>.

speed transmitter devices using InP-based modulators, lasers, or Si-based microring modulators have been demonstrated for industrial applications<sup>39–41</sup>. Effective temperature management is critical for these devices; thus, the incorporation of either a temperature stabilization unit or thermo-optic compensator is necessary<sup>42</sup>. By contrast, our PLZT modulators, which are equipped with balanced phase shifters on MZI arms, demonstrate better thermal insensitivity in modulation. Hence, rather than monitoring the static parameters for the present modulator, measuring dynamic properties associated with signals (e.g., the Q or BER parameters) during exposure of the devices to elevated temperatures is more effective. In these experiments, the modulator was first driven as an OOK transmitter at line rates of 100, 128, and 148 Gbit s<sup>-1</sup>. The corresponding BERs associated with the synthesized signals were determined over the temperature range from 25 to 100 °C. Figure 5 shows that signaling was maintained, with no change in the BER from 25 to 70 °C. The modulation began to be affected by temperature at approximately 80 °C; however, the original performance was completely recovered when the device was cooled to room temperature, even after it was exposed to temperatures as high as 100 °C. As a result, the PLZT modulator could operate at various elevated temperatures without failure, which is a critical aspect of the development of temperature-insensitive optical transmitters and other components suitable for use in harsh environments such as those encountered in B5G, LiDAR, satellite, and avionics applications. Although there have been notable demonstrations of ferroelectric films in optoelectronic devices, to the best of our knowledge, this is the first experimental result for a synthesized PLZT modulator device that ensures the thermal reliability of high-speed modulation across a broad temperature range (25–100 °C)<sup>21,30</sup>.

## Discussion

This work demonstrated the direct spin coating of PLZT thin films having a ferroelectric phase onto the SiO<sub>2</sub> surfaces of Si substrates. The fabricated waveguide modulator exhibited efficient EO modulation with a large Pockels coefficient, together with high-speed signaling capability. A device

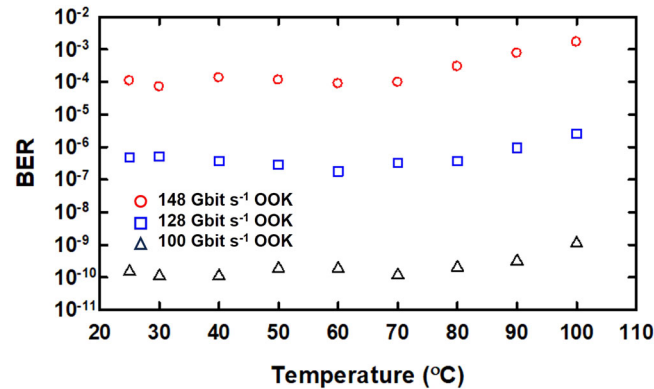


**Fig. 5 | High-speed signaling fidelity for PLZT modulator at elevated temperatures.** The estimated BER values for the synthesized OOK signals from 100 to 148 Gbit s<sup>-1</sup> as functions of the operating temperature as high as 100 °C.

based on this PLZT modulator enabled signaling at line rates as high as 304 Gbit s<sup>-1</sup>. High-speed transmission was demonstrated with a drive voltage of 200 mV<sub>pp</sub>. Reducing the microwave loss associated with the microstrip lines and improving the traveling modulation could further enhance the high-speed performance of this technology. This modulator was capable of transmission at wavelengths of 1310 and 1550 nm.

Table 1 presents a focused comparison of various performance metrics from this study with state-of-the-art values reported in recent years, specifically for waveguide devices using ferroelectric materials fabricated on Si substrates. All ferroelectric modulators provided higher EO coefficients in devices compared to legacy crystal modulators such as LN. The majority of EO modulators are capable of high-speed transmission. EO modulators are mainly formed on structures such as MZIs and microring resonators (MRRs). As shown in Table 1, our device recorded the modulation with the

**Table 1 | Comparison of performance metrics for EO modulators**

Platform	Structure	Line rate (Gbit s <sup>-1</sup> )	Format	Peak-to-peak drive voltage (V)	Half-wave voltage length product (V-mm)	Footprint, diameter ( $\phi$ ) or active length (mm)	EO coefficient (pm V <sup>-1</sup> )	Phase shifter loss (dB mm <sup>-1</sup> )	Operating ( $\Delta T$ ) or storage ( $T$ ) temperature range
PLZT This work	MZI	172	OOK <sup>***</sup>	0.2	7.0 <sup>*</sup> /5.8 <sup>**</sup>	2.5	195	0.6	$\Delta T = 25\text{--}100\text{ }^\circ\text{C}$ $T = 85\text{ }^\circ\text{C}$
		304	PAM4 <sup>*,*</sup>	0.2					
PZT <sup>4</sup>	MRR	40	OOK <sup>*</sup>	4.2	33 <sup>*</sup> /32 <sup>**</sup>	$\phi = 0.2$	67	0.5	n/a
BTO <sup>2</sup>	MRR	40	OOK <sup>*</sup>	n/a	4.5 <sup>*</sup>	$\phi = 0.1$	342	1.0	n/a
BTO <sup>24,29</sup>	MZI	25 $\sim$ 128	OOK <sup>*</sup>	1.0 $\sim$ 2.0	2.3 $\sim$ 7.2 <sup>*</sup>	2.0	380	0.6	n/a
		212	PAM4 <sup>*</sup>	0.83					
BTO <sup>30,44</sup>	Plasmonic	72 $\sim$ 216	OOK <sup>*</sup>	1.8 $\sim$ 2.8	0.048 $\sim$ 0.2 <sup>*</sup>	0.01 $\sim$ 0.015	n/a	$1.5 \times 10^3$	$\Delta T = 20\text{--}130\text{ }^\circ\text{C}$
		116 $\sim$ 256	PAM4 <sup>*</sup>	1.8 $\sim$ 2.8					
SOH <sup>43</sup>	MZI	150	OOK <sup>*</sup>	0.81	0.5 <sup>*</sup>	0.75	150	n/a	$T = 85\text{ }^\circ\text{C}$
		280	PAM4 <sup>*</sup>	0.86					
SOH <sup>16</sup>	MZI	40	OOK <sup>*</sup>	1.7	3.3 <sup>*</sup>	1.5	80	1.7	$T = 85\text{ }^\circ\text{C}$
SPH <sup>12</sup>	MZI	120	OOK <sup>*</sup>	2.0	14 <sup>*</sup>	8.0	223	0.2	$\Delta T = 25\text{--}110\text{ }^\circ\text{C}$
		200	PAM4 <sup>*</sup>	1.3					

SOH Si and organic hybrid modulator, SPH Si and polymer hybrid modulator, n/a not available.

Operating wavelength: \*1510 nm and \*\*1310 nm.

highest line rates (172 Gbit s<sup>-1</sup> OOK and 304 Gbit s<sup>-1</sup> PAM4). We highlight the unique and distinctive method used to prepare PLZT films via a simple spin-coating technique through a sol-gel chemical reaction. The technique not only simplifies the fabrication of modulators on a Si substrate but also shows great promise in terms of scalability. Because the electrically induced dipole in PLZT is well stabilized, a notable advantage of our PLZT modulator is its ability to operate without further DC electric poling control. The MRR offers the benefit of a compact footprint and easy integration into other photonic circuits; however, it has a limited EO bandwidth because of the finite photon lifetimes in the high-quality-factor resonator. The plasmonic BTO modulator is a unique device that features an ultra-small footprint. The measured  $V_\pi$  and drive peak-to-peak voltages are moderate compared to those of other modulators. However, significantly large optical propagation loss is a concern, making length control of the phase shifter difficult.

From a similar perspective of device fabrication efficiency, a comparison with organic polymer modulators is interesting. Notably, Si and polymer hybrid modulators have demonstrated outstanding performance in terms of high-speed operation, drive voltage, device size, and thermal stability<sup>43</sup>. The recent development of EO polymers with high glass-transition temperatures has led to enhanced device reliability, paving the way for a technology that supports highly scalable transmitters with line rates exceeding 200 Gbit s<sup>-1</sup><sup>12,16</sup>. However, managing the laser power remains a concern for device operation because of material stability issues related to photoinduced oxidation and radical reactions<sup>45</sup>.

From the device information listed in Table 1, we conclude that the PLZT modulator demonstrated here achieves excellent optical modulation characteristics. The PLZT exhibits high transparency at telecommunication wavelengths sufficiently distant from the material's bandgap<sup>46</sup>. We confirmed the stability of the PLZT modulator against the incident laser, observing no degradation in device properties throughout the experiment. More comprehensive and systematic reliability tests are planned for the future.

While significant advancements are anticipated in the development of ultra-high-speed modulation at telecom wavelengths, other applications at visible to near-infrared wavelengths have recently been attracting attention in optical imaging<sup>47,48</sup>, optogenetics<sup>49</sup>, and quantum science and technology<sup>50,51</sup>. A PLZT thin film has wide transparency in this wavelength region and enables fast modulation of optical signals in the waveguide structure. This work builds on the fabrication of the PLZT thin films on insulators and photonics applications because of its large EO coefficient,

controllable refractive index, and high-frequency response. These properties are central to a wide range of light-control and photonics applications.

## Methods

### PLZT preparation and device fabrication

Intermediate layers were prepared on the substrate by spin coating a solution of La(NO<sub>3</sub>)<sub>3</sub> in 2-methoxyethanol. The substrate was heated at 300 °C to remove the residual solvent and then at 500 °C for 15 min. The film thickness was less than 10 nm. The unit-cell parameter obtained by XRD analysis is  $a = 4.07\text{ \AA}$ , consistent with the value expected for crystalline La<sub>2</sub>O<sub>3</sub>. Remarkably, this value represented a mismatch of only 0.7% relative to the unit-cell parameter for PLZT. A PLZT precursor solution (Pb<sub>1-x</sub>La<sub>x</sub>(Zr<sub>y</sub>Ti<sub>1-y</sub>)<sub>1-x/4</sub>O<sub>3</sub>,  $x/y/(1-y) = 8.0/65/35$ <sup>32</sup>) was spin-coated onto the La<sub>2</sub>O<sub>3</sub>-coated substrate. A crystalline film was obtained after the spin-coated film was heated at 300 °C for 5 min in air, followed by additional heating at 600 °C for 15 min under O<sub>2</sub>. This procedure gave a PLZT film with a thickness of approximately 100 nm. This same process was repeated to obtain samples with thicknesses between 300 and 500 nm.

An MZI waveguide structure was fabricated on the PLZT layer using electron beam lithography (Elionix, ELS-G100) followed by dry chemical etching (SAMCO, NR10) using Ar and CHF<sub>3</sub>. Coplanar Au strip-line electrodes, each 20 μm wide and 1.5 μm thick, were subsequently deposited onto the device using electroplating techniques. A 1 μm-thick SiO<sub>2</sub> layer was subsequently deposited as a top cladding via chemical vapor deposition (SAMCO, PD-100). The propagation loss for the PLZT waveguide was 0.66 dB mm<sup>-1</sup> (Supplementary Fig. 6). The on-chip loss for the fabricated MZI modulator was estimated to be 5.6 dB, comprising a phase-shifter loss of 1.7 dB and other passive component losses of 3.9 dB. To activate the EO effect, electric poling in the voltage range from 70 to 150 V was applied between the electrodes at 90 °C to induce polarization.

### Device characterization

Both  $V_\pi$  and modulation efficiency values were obtained using a function generator with a sinusoidal electric signal with a frequency of 14 kHz. During these measurements, laser light from a wavelength-tunable laser (Santec, TSL-550) was guided to the modulators through a polarization-maintaining fiber. The optical signal from the modulator was coupled to a single-mode fiber and sent to a photodetector (Thorlabs, DPA10CS) whose signal was recorded using an oscilloscope. The  $V_\pi L$  values measured at various wavelengths are shown in Supplementary Fig. 7. On the basis of the experimental  $V_\pi$  values, we calculated the in-device EO coefficient for the

modulator using the equation  $r_{\text{eff}} = (1/2)\lambda d/(n^3 V_{\pi} L I)$ , where  $\lambda$  is the wavelength,  $d$  is the electrode gap,  $n$  is the effective refractive index, and  $I$  is the optical and electrical overlap integral factor. Using these parameters, we obtained an  $r_{\text{eff}}$  of 195 pm V<sup>-1</sup>. To measure the modulation frequency response, a vector network analyzer (Anritsu, MS4647B) with a signaling range of 1–70 GHz was used to characterize the EO 3-dB bandwidth ( $S_{21}$ ). The modulated output signal was received by an O/E calibration module (Anritsu, MN4765B-0072). An RF probe (FormFactor, I67-A-GSG) was used to introduce the signal to the traveling-wave electrode on the modulator while a second probe was attached to the end of the electrode with a 50 Ω termination to avoid power reflections.

### High-speed modulation assessment

The experimental setup employed during the high-bit-rate experiments is illustrated in Fig. 4a. In these experiments, OOK signals were generated by producing electrical signals from an AWG (Keysight, M8199B) with an analog bandwidth of 80 GHz and operating at 256 GSa s<sup>-1</sup> in conjunction with a power setting using a linear driver (SHF, T850C). In our experimental setup, the drive signals of OOK and PAM4 were applied to the modulator with voltage swings ranging from 100 to 270 mV (Supplementary Fig. 8). Nyquist PAM4 signals were generated by operating the AWG at rates as high as 304 Gbit s<sup>-1</sup>. To detect the synthesized OOK and PAM4 signals, the optical signals were pre-amplified using an Er-doped fiber amplifier (EDFA, Amomics, AEDFA-40) at 1550 nm before they were directed to a photodetector (Finisar, XPDV3320R). A Pr-doped fiber amplifier (PDFA, FiberLabs, AMP-FL8612) was also used for transmission at a wavelength of 1310 nm. Digital communication analyzer high-speed oscilloscopes (Keysight, DCA-X N100A and N1030A, 95 GHz) and a real-time oscilloscope (Keysight, RTO UXR0702AP, 70 GHz) were used during these experiments. The collected signals were processed using Bessel low-pass filtering and linear feedforward equalization techniques. The high-speed modulations were independent of the wavelengths of the lasers used in this study (Supplementary Fig. 7).

### Evaluation of high-temperature stability

We examined the effects of temperature on modulation by investigating the high-speed performance of the PLZT modulator at various elevated temperatures. During these tests, the modulator was mounted on a thermoelectric device that enabled the operating temperature to be adjusted within the range from 20 to 100 °C while maintaining the optical and electrical connections. In an additional test assessing long-term high-temperature storage, the device was heated at 85 °C in air without optical or electrical connections. After various time periods, these connections were again activated to assess the modulation efficiency.

### Data availability

The datasets that support the findings of this study are available on request from the corresponding author (S.Y.)

### Code availability

The algorithms used for this study are standard and are outlined in “Method”. Code sprits can be provided by the corresponding author (S.Y.)

Received: 31 January 2024; Accepted: 25 June 2024;

Published online: 01 July 2024

### References

- Wang, C. et al. Integrated lithium niobate electro-optic modulators operating at CMOS-compatible voltages. *Nature* **562**, 101–104 (2018).
- Abel, S. et al. Large Pockels effect in micro- and nanostructured barium titanate integrated on silicon. *Nat. Mater.* **18**, 42–47 (2019).
- Hamze, A. K., Reynaud, M., Geler-Kremer, J. & Demkov, A. A. Design rules for strong electro-optic materials. *npj Comput. Mater.* **6**, 130 (2020).
- Alexander, K. et al. Nanophotonic Pockels modulators on a silicon nitride platform. *Nat. Commun.* **9**, 2444 (2018).
- He, M. et al. High-performance hybrid silicon and lithium niobate Mach-Zehnder modulators for 100 Gbit s<sup>-1</sup> and beyond. *Nat. Photon.* **13**, 359–365 (2019).
- Zhu, D. et al. Integrated photonics on thin-film lithium niobate. *Adv. Opt. Photon.* **13**, 242–352 (2021).
- Li, Z. et al. High density lithium niobate photonic integrated circuits. *Nat. Commun.* **14**, 4856 (2023).
- Weigel, P. et al. Bonded thin film lithium niobate modulator on a silicon photonics platform exceeding 100 GHz 3-dB electrical modulation bandwidth. *Opt. Exp.* **26**, 23728–23739 (2018).
- Chen, G. et al. High performance thin-film lithium niobate modulator on a silicon substrate using periodic capacitively loaded traveling-wave electrode. *APL Photon.* **7**, 026103 (2022).
- Haffner, C. et al. Low-loss plasmon-assisted electro-optic modulator. *Nature* **556**, 483–486 (2018).
- Wolf, S. et al. Silicon-organic hybrid (SOH) Mach-Zehnder modulators for 100 Gbit s<sup>-1</sup> on-of keying. *Sci. Rep.* **8**, 2598 (2018).
- Lu, G. et al. High-temperature-resistant silicon-polymer hybrid modulator operating at up to 200 Gbit s<sup>-1</sup> for energy-efficient datacentres and harsh-environment applications. *Nat. Commun.* **11**, 4224 (2020).
- Baeuerle, B. et al. 120 GBd plasmonic Mach-Zehnder modulator with a novel differential electrode design operated at a peak-to-peak drive voltage of 178 mV. *Opt. Exp.* **27**, 16823–16832 (2019).
- Eschenbaum, C. et al. Thermally stable silicon-organic hybrid (SOH) Mach-Zehnder modulator for 140 GBd PAM4 transmission with sub-1 V drive signals. In *Proc. European Conference on Optical Communication (ECOC) 2022*, Th3B.2 (IEEE, 2022).
- Miura, H. et al. High thermal stability 40 GHz electro-optic polymer modulators. *Opt. Exp.* **25**, 28643–28649 (2017).
- Kieninger, C. et al. Demonstration of long-term thermally stable Silicon-Organic Hybrid Modulators at 85 °C. *Opt. Exp.* **26**, 27955–27964 (2018).
- Meng, X. Y., Wang, Z. Z., Zhu, Y. & Chen, C. T. Mechanism of the electro-optic effect in the perovskite-type ferroelectric KMbO<sub>3</sub> and LiNbO<sub>3</sub>. *J. Appl. Phys.* **101**, 103506 (2007).
- Zgonik, M. et al. Materials constants of KNbO<sub>3</sub> relevant for electro- and acousto-optics. *J. Appl. Phys.* **74**, 1287–1297 (1993).
- Kim, D. M. et al. Thickness dependence of structural and piezoelectric properties of epitaxial Pb(Zr<sub>0.52</sub>Ti<sub>0.48</sub>)O<sub>3</sub> films on Si and SrTiO<sub>3</sub> substrates. *Appl. Phys. Lett.* **88**, 142904 (2006).
- Karvounis, A., Timpu, F., Vogler-Neuling, V. V., Savo, R. & Grange, R. Barium Titanate nanostructures and thin films for photonics. *Adv. Opt. Mater.* **8**, 2001249 (2020).
- Abel, S. et al. A strong electro-optically active lead-free ferroelectric integrated on silicon. *Nat. Commun.* **4**, 1671 (2013).
- Wan, X. et al. Refractive indices and linear electro-optic properties of (1-x)Pb(Mg<sub>1/3</sub>Nb<sub>2/3</sub>)O<sub>3</sub>-xPbTiO<sub>3</sub> single crystals. *Appl. Phys. Lett.* **85**, 5233–5235 (2004).
- Abe, S., Joichi, T., Uekusa, K., Hara, H. & Masuda, S. Photonic integration based on a ferroelectric thin-film platform. *Sci. Rep.* **9**, 16548 (2019).
- Eltes, F. et al. A BaTiO<sub>3</sub>-based electro-optic Pockels modulator monolithically integrated on an advanced silicon photonics platform. *J. Lightwave Technol.* **37**, 1456–1462 (2019).
- Alam, M. S. et al. Net 220 Gbps/λ IM/DD transmission in O-band and C-band with silicon photonic traveling-wave MZM. *J. Lightwave Technol.* **39**, 4270–4278 (2021).
- Jiao, H. et al. Ferroelectric field effect transistors for electronics and optoelectronics. *Appl. Phys. Rev.* **10**, 011210 (2023).
- Nguyen, M. D., Nguyen, C. T. Q., Vu, H. N. & Rijnders, G. Experimental evidence of breakdown strength and its effect on energystorage performance in normal and relaxor ferroelectric films. *Curr. Appl. Phys.* **19**, 1040–1045 (2019).

28. Eltes, F. et al. An integrated optical modulator operating at cryogenic temperatures. *Nat. Mater.* **19**, 1164–1168 (2020).

29. Eltes, F. et al. Thin-film BTO-based modulators enabling 200 Gb s<sup>-1</sup> data rates with sub 1 V<sub>pp</sub> drive signal. In *Proc. 2023 Optical Fiber Communication (OFC) Conference*, ThA.2 (Optica Publishing Groups, 2023).

30. Messner, A. et al. Plasmonic ferroelectric modulators. *J. Lightwave Technol.* **37**, 281–290 (2019).

31. Haerting, G. H. & Land, C. E. Hot-pressed (Pb, La)(Zr, Ti)O<sub>x</sub> ferroelectric ceramics for electrooptic applications. *J. Am. Ceram. Soc.* **54**, 1–11 (1971).

32. Huang, C. et al. Large quadratic electro-optic effect of the PLZT thin films for optical communication integrated devices. *ACS Photon.* **7**, 3166–3176 (2020).

33. Yoon, D. S., Kim, C. J., Lee, J. S., Lee, W. J. & No, K. Epitaxial growth of sol-gel PLZT thin films. *J. Mater. Res.* **9**, 420–425 (1994).

34. Yu, J., Meng, X. J., Sun, J. L., Huang, Z. M. & Chu, H. J. Optical and electrical properties of highly (100)-oriented PbZr<sub>1-x</sub>Ti<sub>x</sub>O<sub>3</sub> thin films on the LaNiO<sub>3</sub> buffer layer. *J. Appl. Phys.* **96**, 2792–2799 (2004).

35. George, J. et al. Lanthanide-assisted deposition of strongly electro-optic PZT thin films on silicon: toward integrated active nanophotonic devices. *ACS Appl. Mater. Interfaces* **7**, 13350–13359 (2015).

36. Tang, P., Towner, D. J., Hamano, T. & Meier, A. L. Electrooptic modulation up to 40 GHz in a barium titanate thin film waveguide modulator. *Opt. Exp.* **12**, 5962–5967 (2004).

37. Lederer, D. & Raskin, J.-P. Effective resistivity of fully-processed SOI substrates. *Solid-State Electron.* **49**, 491–496 (2005).

38. Neve, C. R. et al. Impact of neutron irradiation on the RF properties of oxidized high-resistivity silicon substrates with and without a trap-rich passivation layer. *Microelectron. Reliab.* **51**, 326–331 (2011).

39. Ozaki, J. et al. 500-Gb s<sup>-1</sup> λ<sup>-1</sup> Operation of ultra-low power and low-temperature-dependence InP-based high-bandwidth coherent driver modulator. *J. Lightwave Technol.* **38**, 5086–5091 (2020).

40. Lange, S. et al. 100 GBd Intensity modulation and direct detection with an InP-based monolithic DFB laser Mach–Zehnder modulator. *J. Lightwave Technol.* **36**, 97–102 (2018).

41. Fathololoumi, S. et al. 1.6 Tbps silicon photonics integrated circuit and 800 Gbps photonic engine for switch co-packaging demonstration. *J. Lightwave Technol.* **39**, 1155–1161 (2021).

42. Timurdogan, E. et al. An ultralow power athermal silicon modulator. *Nat. Commun.* **5**, 4008 (2014).

43. Eschenbaum, C. et al. Thermally stables silicon-organic hybrid (SOH) Mach-Zehnder modulator for 140 GBd PAM4 transmission with sub-1 V drive signals. In *Proc. European Conference on Optical Communication*, Th3B.2 (IEEE, 2022).

44. Kohli, M. et al. Plasmonic ferroelectric modulator monolithically integrated on SiN for 216 GBd data transmission. *J. Lightwave Technol.* **41**, 3825–3831 (2023).

45. DeRosa, M. E., He, M., Cites, J. S., Garner, S. M. & Tang, Y. R. Photostability of high  $\mu\beta$  electro-optic chromophores at 1550 nm. *J. Phys. Chem. B* **108**, 8725–8730 (2004).

46. Batra, V., Kotru, S., Varagas, M. & Ramana, C. V. Optical constants and band gap determination of Pb<sub>0.95</sub>La<sub>0.05</sub>Zr<sub>0.54</sub>Ti<sub>0.46</sub>O<sub>3</sub> thin films using spectroscopic ellipsometry and UV-visible spectroscopy. *Opt. Mater.* **49**, 123–128 (2015).

47. Wu, C. et al. Enhancing optical nonlinearity in a nonstoichiometric SiN waveguide for cross-wavelength all-optical data processing. *ACS Photon.* **2**, 1141–1154 (2015).

48. Rank, E. A. et al. Toward optical coherence tomography on a chip: in vivo three-dimensional human retinal imaging using photonic integrated circuit-based arrayed waveguide gratings. *Light Sci. Appl.* **10**, 1–15 (2021).

49. Shim, E., Chen, Y., Masmanidis, S. & Li, M. Multisite silicon neural probes with integrated silicon nitride waveguides and gratings for optogenetic applications. *Sci. Rep.* **6**, 22693 (2016).

50. Niffenegger, R. J. et al. Integrated multi-wavelength control of an ion qubit. *Nature* **586**, 538–542 (2020).

51. Mehta, K. K. et al. Integrated optical multi-ion quantum logic. *Nature* **586**, 533–537 (2020).

## Acknowledgements

This work was supported, in part, by a Japan Society for the Promotion of Science Grant-in-Aid for Scientific Research, Ministry of Education, Culture, Sports, Science and Technology (MEXT), under Grant No. JP23H00188; Japan Science and Technology Agency, under Grant No. JPMJMS2063; National Institute of Information and Communications Technology, under Grant No. 02101; and Cooperative Research Programs “Network Joint Research Center for Material and Device” and “Dynamic Alliance for Open Innovation Bridging Human, Environment, and Materials” of MEXT.

## Author contributions

J.M., F.U., G.L., and S.Y. developed the idea and conceived the experiment. J.M., H.S., and S.Y. conceived the device design. J.M., F.U., and S.A.Y. fabricated the devices. J.M., Y.Y., and H.S. performed numerical simulation. J.M., F.U., S.A.Y., Y.Y., and S.Y. carried out the experiments. J.M. and S.Y. wrote the manuscript with contributions from all authors. S.Y. supervised the project.

## Competing interests

The authors declare no competing interests.

## Additional information

**Supplementary information** The online version contains supplementary material available at <https://doi.org/10.1038/s43246-024-00558-5>.

**Correspondence** and requests for materials should be addressed to Shiyoshi Yokoyama.

**Peer review information** *Communications Materials* thanks the anonymous reviewers for their contribution to the peer review of this work. Primary Handling Editor: John Plummer. A peer review file is available.

**Reprints and permissions information** is available at <http://www.nature.com/reprints>

**Publisher's note** Springer Nature remains neutral with regard to jurisdictional claims in published maps and institutional affiliations.

**Open Access** This article is licensed under a Creative Commons Attribution 4.0 International License, which permits use, sharing, adaptation, distribution and reproduction in any medium or format, as long as you give appropriate credit to the original author(s) and the source, provide a link to the Creative Commons licence, and indicate if changes were made. The images or other third party material in this article are included in the article's Creative Commons licence, unless indicated otherwise in a credit line to the material. If material is not included in the article's Creative Commons licence and your intended use is not permitted by statutory regulation or exceeds the permitted use, you will need to obtain permission directly from the copyright holder. To view a copy of this licence, visit <http://creativecommons.org/licenses/by/4.0/>.

© The Author(s) 2024